AGU PUBLICATIONS

JGR

Journal of Geophysical Research: Planets

RESEARCH ARTICLE

10.1002/2014JE004628

Key Points:
- Soft X-ray imaging infers total lunar limb column density
- The SWCX signal is dominated by exospheric species of solar wind origin
- SWCX with the lunar exosphere was observed by ROSAT

Correspondence to:
M. R. Collier,
michael.r.collier@nasa.gov

Citation:
Collier, M. R., et al. (2014), On lunar exospheric column densities and solar wind access beyond the terminator from ROSAT soft X-ray observations of solar wind charge exchange, *J. Geophys. Res. Planets, 119*, 1459–1478, doi:10.1002/2014JE004628.

Received 1 MAR 2014
Accepted 15 MAY 2014
Accepted article online 22 MAY 2014
Published online 3 JUL 2014

The copyright line for this article was changed on 22 October 2014.

On lunar exospheric column densities and solar wind access beyond the terminator from ROSAT soft X-ray observations of solar wind charge exchange

Michael R. Collier[1,2], S. L. Snowden[1], M. Sarantos[1,2,3], M. Benna[3], J. A. Carter[4], T. E. Cravens[5], W. M. Farrell[1,2], S. Fatemi[6], H. Kent Hills[7], R. R. Hodges[2,8], M. Holmström[6], K. D. Kuntz[9], F. Scott Porter[1], A. Read[4], I. P. Robertson[5], S. F. Sembay[4], D. G. Sibeck[1], T. J. Stubbs[1,2,3], P. Travnicek[10], and B. M. Walsh[1,3]

[1]NASA Goddard Space Flight Center, Greenbelt, Maryland, USA, [2]DREAM, Lunar Science Institute, NASA Ames Research Center, Moffett Field, California, USA, [3]Goddard Earth Science and Technology Center, University of Maryland, Baltimore County, Catonsville, Maryland, USA, [4]Department of Physics and Astronomy, Leicester University, Leicester, UK, [5]Department of Physics and Astronomy, University of Kansas, Lawrence, Kansas, USA, [6]Swedish Institute of Space Physics, Kiruna, Sweden, [7]QSS Group Inc., Merrifeld, Virginia, USA, [8]Laboratory for Atmospheric and Space Physics, University of Colorado, Boulder, Boulder, Colorado, USA, [9]Department of Physics and Astronomy, Johns Hopkins University, Baltimore, Maryland, USA, [10]Institute of Atmospheric Physics, Academy of Sciences, Prague, Czech Republic

Abstract We analyze the Röntgen satellite (ROSAT) position sensitive proportional counter soft X-ray image of the Moon taken on 29 June 1990 by examining the radial profile of the surface brightness in three wedges: two 19° wedges (one north and one south) 13–32° off the terminator toward the dark side and one wedge 38° wide centered on the antisolar direction. The radial profiles of both the north and the south wedges show significant limb brightening that is absent in the 38° wide antisolar wedge. An analysis of the soft X-ray intensity increase associated with the limb brightening shows that its magnitude is consistent with that expected due to solar wind charge exchange (SWCX) with the tenuous lunar atmosphere based on lunar exospheric models and hybrid simulation results of solar wind access beyond the terminator. Soft X-ray imaging thus can independently infer the total lunar limb column density including all species, a property that before now has not been measured, and provide a large-scale picture of the solar wind-lunar interaction. Because the SWCX signal appears to be dominated by exospheric species arising from solar wind implantation, this technique can also determine how the exosphere varies with solar wind conditions. Now, along with Mars, Venus, and Earth, the Moon represents another solar system body at which SWCX has been observed.

1. Introduction

The notion that the Moon produces observable X-rays predates the Apollo era. The proposed generation mechanisms in this early work were magnetospheric or solar wind electrons. For example, *Haymes and Juday* [1965] used the existence of bremsstrahlung X-rays from precipitating electrons in the auroral zone to predict that the full moon, that is, the Moon in the magnetotail, will have an X-ray surface brightness comparable to the high-latitude atmosphere during aurora. They also discussed X-ray generation from solar wind electrons as well as the possibility of X-rays generated by lunar traversals of Earth's plasma sheet.

On the observational side, *Giacconi et al.* [1962] attempted to, but did not, observe fluorescence X-rays produced on the lunar surface from solar X-rays. However, it was not until 29 June 1990 that the Röntgen satellite (ROSAT) X-ray telescope [*Trümper*, 1993] made the first soft X-ray image of the Moon [*Schmitt et al.*, 1991]. Surprisingly, soft X-rays were observed even on the nightside of the Moon where their presence could not be ascribed to scattered solar X-rays, the scattering process being too inefficient on the nightside. At the time, the ROSAT observations of soft X-rays on the dark side of the Moon were believed to be due to continuum emission from solar wind electrons with energies of a few hundred electron volts impacting the lunar surface and depositing their energy in the outermost lunar regolith producing bremsstrahlung continuum soft X-ray emission in the process.

Many years later, however, ROSAT observed another solar system object, a comet, with surprising results. This 20 ks observation, made in late March of 1996, was of comet Hyakutake, and it showed that the comet

emitted a copious flux of soft X-rays [*Lisse et al.*, 1996]. This was a mystery at that time because comets are not associated with hot plasma, very energetic particles, or optically thick material that could scatter X-rays from an external source, e.g., the Sun. The original interpretation of the comet Hyakutake observation was that the emitted soft X-rays were associated with the comet's interaction with the solar wind, likely continuum emission from electron bremsstrahlung.

Shortly thereafter, *Cravens* [1997] proposed that the soft X-ray emission was in fact line emission due to charge exchange between heavy solar wind ions and cometary neutrals. In this mechanism, known as SWCX (pronounced "swicks") for solar wind charge exchange, a heavy highly charged solar wind ion (e.g., O^{7+}) captures an electron from a neutral atom or molecule. The heavy ion is left in an excited state and emits a photon in the extreme ultraviolet or soft X-ray energy range (~1 keV). Although the high charge state heavy ion component of the solar wind is about 0.1% by number density, the solar wind flux is tremendously high ($\sim 3 \times 10^8/\mathrm{cm}^2/\mathrm{s}$) so that the heavy ion flux in the solar wind is considerable.

Since the original observations of comet Hyakutake, SWCX soft X-ray emission has been observed at other comets [e.g., *Krasnopolsky et al.*, 2004; *Cravens*, 2002] and other solar system bodies including Mars and Venus [*Gunell et al.*, 2004; *Dennerl*, 2002, 2008; *Dennerl et al.*, 2002; *Holmström and Kallio*, 2004; *Holmström et al.*, 2001; *Bhardwaj et al.*, 2007], as well as from larger-scale heliospheric structures such as the helium focusing cone [*Koutroumpa et al.*, 2009]. In particular, SWCX between the shocked solar wind plasma in the magnetosheath and the terrestrial exosphere produces soft X-ray emission observable on scientifically relevant timescales [*Cravens et al.*, 2001; *Collier et al.*, 2010] through the same charge exchange mechanism that has allowed imaging of magnetopause motion using energetic neutral atoms [e.g., *Collier et al.*, 2005a; *Taguchi et al.*, 2005; *Robertson et al.*, 2006; *Hosokawa et al.*, 2008].

This aspect of SWCX soft X-ray emission, viz., near-Earth emission, became particularly clear after multiple observations of the Hubble Deep Field-North by XMM-Newton taken over a 2 week period from late May to early June 2001 reported by *Snowden et al.* [2004]. Three of the observations were spectrally statistically identical and consistent with the cosmic background. The fourth observation, taken by chance when the solar wind flux observed near Earth was about an order of magnitude higher than nominal (up to about $30 \times 10^8/\mathrm{cm}^2/\mathrm{s}$), showed clear lines associated with high charge state oxygen, neon, and magnesium, indicative of SWCX soft X-ray emission in the Earth's vicinity.

In 2001, two sets of observations of the Moon were made by the Chandra X-Ray Observatory which detected time-variable soft X-ray emission that consisted primarily of lines from O^{+6} and O^{+7} when viewing the optically dark side [*Wargelin et al.*, 2004]. The Chandra observations coupled with simultaneous solar wind measurements showed that SWCX was in fact the soft X-ray emission mechanism responsible for the dark side flux observed by Chandra and therefore ROSAT. In particular, it was shown that the predicted *geocoronal* emission matched the Chandra observations extremely well so that the majority of the emission was in fact solar wind charge exchange with the terrestrial exosphere occurring between the Earth and the Moon (the Moon is at about 60 Earth radii)

However, it is expected that not all of the (nonscattered) soft X-ray emission detected when observing the Moon is due to solar wind charge exchange with the terrestrial exosphere. This is, in part, because the Moon itself has a tenuous atmosphere, strictly speaking an exosphere, which (although predicted prior to, e.g., *Gott and Potter* [1970]) was first observed by Apollo program instrumentation [*Stern*, 1999]. To date, only He, Ar^{40}, K, Na, and Rn^{222} have been firmly identified in the lunar exosphere where they arise from the solar wind (He), the lunar regolith (K and Na), and the lunar interior (Ar^{40} and Rn^{222}). However, upper limits have been set for a large number of other species. The highest densities observed have been from He and Ar [see *Stern*, 1999, Table 1], both of which show a large variation with solar zenith angle with helium peaking on the nightside at a density of about $4 \times 10^4\ \mathrm{cm}^{-3}$ and argon peaking near the terminator at a density $\sim 10^5\ \mathrm{cm}^{-3}$.

The longitudinal behavior of the helium concentration results from the particles in the lunar exosphere that are not adsorbed onto the surface spending more time on the cold nightside than on the warmer dayside because the lateral extent of their ballistic trajectories is proportional to temperature [e.g., *Hodges*, 1973, 1975]. Conversely, the longitudinal behavior of the argon concentration results from a surface interaction, an excess of adsorption over desorption on the nightside as the lunar surface cools [*Hodges*, 1977]. NASA's recently launched Lunar Atmosphere and Dust Environment Explorer (LADEE) mission will help to further determine the constituents of the lunar atmosphere [*Elphic et al.*, 2011; *Mahaffy et al.*, 2009].

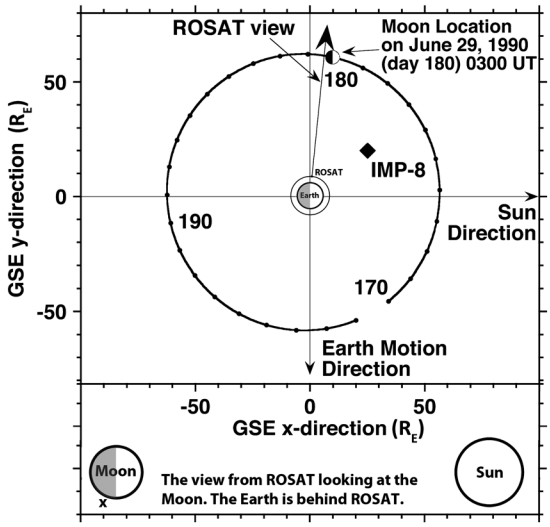

Figure 1. This figure shows the geometry between ROSAT, Earth, the Moon, and the Sun during the observation on 29 June 1990. (top) The view looking toward the GSE *-z* direction. ROSAT is in low Earth orbit and hence near the origin. The Moon is at about 60 Earth radii along the positive GSE *y* axis. The Sun is to the right in this figure. (bottom) The view from ROSAT looking at the Moon with Earth behind the satellite. Note that any point on the lunar circumference in this view defines a look direction path from ROSAT that is tangential to the lunar surface. The "x" in this panel is approximately 13° from the terminator and indicates in this view the axis of the ROSAT line of sight that extends in and out of the page. The position of IMP-8 at the time of the ROSAT observation, just a few tens of R_E from the Moon, is also indicated on the plot.

Thus, some soft X-ray emission will result from the interaction between the solar wind and the tenuous lunar exosphere while the Moon is outside Earth's magnetosphere in the solar wind and is being bombarded by high charge state heavy solar wind ions. The soft X-ray intensities produced by this process have been modeled by *Robertson et al.* [2009]. Although their simulations assumed an observation point on the lunar surface, specifically at the lunar pole, their predicted X-ray fluxes were comparable to other sources of diffuse X-rays including the diffuse cosmic X-ray background which is typically ~ 10 keV/cm^2/s/sr [*Lumb et al.*, 2002]. Consequently, the Robertson et al. results indicate that the flux of solar wind charge exchange soft X-rays from the solar wind interaction with the lunar exosphere itself is large enough to be observable.

Here we report an analysis of the 29 June 1990 ROSAT observation of the Moon. There was an additional, shorter, ROSAT observation of the Moon on 9 March 1991 that was primarily an occultation experiment [*Predehl et al.*, 1992], so there is a high energy source in the data. Consequently, we did not use this observation. In the 29 June 1990 observation, we find the expected signatures of lunar exospheric SWCX emission manifest as limb brightening in the ROSAT soft X-ray image of the Moon. The intensity of the emission is consistent with models of the lunar exosphere and simulations of solar wind heavy ion access into the lunar nightside.

2. ROSAT Observations

Figure 1 shows the relationship between ROSAT, the Earth, and the Moon during the period of the observation. The observed flux is comprised of four distinct emission components. Scattered solar X-rays provide the strong enhancement of the sunlit side of the Moon. Exospheric soft X-ray emission resulting from solar wind charge exchange with the terrestrial exosphere covers the entire field with a relatively uniform flux and is the dominant emission component in the direction of the dark Moon. The cosmic soft X-ray diffuse background covers the entire field except where shadowed by the Moon and dominates the off-Moon flux. The emission that is the subject of this paper, namely, solar wind charge exchange with the tenuous lunar atmosphere, appears as a faint limb brightening on the edge of the Moon in the dark side direction from the terminator.

The data analyzed are from the ROSAT Position Sensitive Proportional Counter (PSPC), a circular detector 8 cm in diameter with a 2° field of view. The effective area of the mirror is 220 cm^2 at 0.28 keV [*Snowden et al.*, 1997], and the ROSAT Moon observation itself lasted about 2500 s. However, the PSPC was collecting data for only about 1900 s of that period. In addition, as the Moon moved through ROSAT's field of view, part of the exposure of the Moon occurred when it was off axis. The X-ray telescope's sensitivity is not uniform over the field of view (known as "vignetting"), and this effect was corrected for in the calculations. Consequently, the effective exposure time, correcting to the effective area at the optical axis and including the effect of the window support structure, was about 1400 s. The data analyzed here (weighted by the instrumental response) are for the C-band (1/4 keV), where most of the solar wind charge exchange soft X-ray emission is expected to lie.

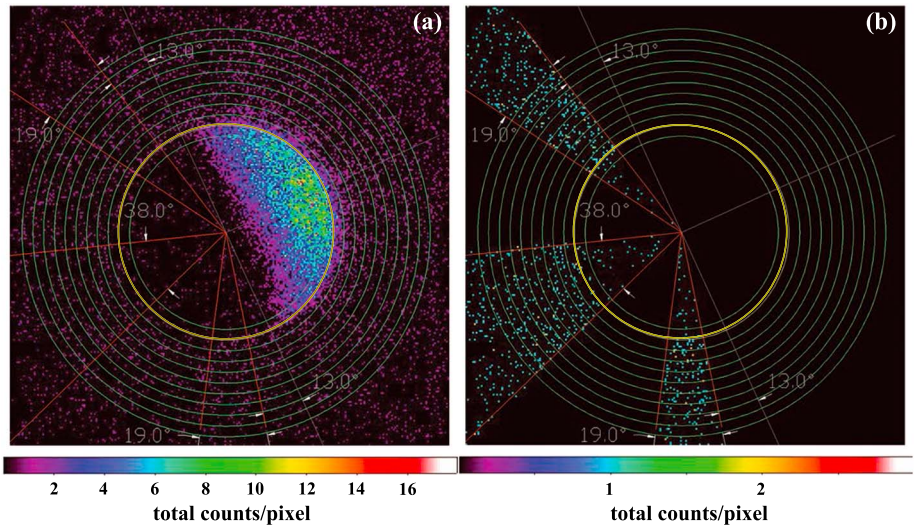

Figure 2. The Moon in soft X-rays as observed by the ROSAT PSPC. (a) All data and the wedges used in the analysis in this paper. (b) The counts appearing in each of the three wedges. Note that the scales are different for Figures 2a and 2b. The yellow circle is at one lunar radius.

The ROSAT image of the Moon has better counting statistics but lower spectral resolution than the Chanda images taken in July and September of 2001 [*Wargelin et al.*, 2004]. So it would not be possible to perform an analysis similar to the one described here on the Chandra images.

Figure 2a shows the ROSAT observations of the Moon analyzed in this paper. The pixels are color coded according to the color scale below the image according to the number of photons observed within each pixel. As is the case for optical images, the bright region in the upper right quadrant is the subsolar point with the brightness due to scattered solar X-rays. The yellow circle is one lunar radius, and the concentric green circles are at intervals of 0.1 lunar radii. During this observation in the 1/4 keV band on the dark side of the Moon, ROSAT observed 4195 counts/s/sr, which are attributable to SWCX with the terrestrial exosphere.

Three wedges are identified in Figure 2a (as well as Figure 2b). There are two wedges, a north and a south wedge, starting from 13° off the terminator. Figure 2b shows only the counts observed in these wedges with the color bar adjusted accordingly. Because we cannot differentiate between scattered solar X-rays and charge exchange X-rays with the spectral capabilities of the PSPC, we are limited to considering data that originate in shadow to avoid scattered solar X-rays. This angle, 13°, was picked mainly based on a visual examination of the image to assess how far behind the terminator one needs to go to avoid scattered solar X-rays while staying close enough to the terminator to assure solar wind access to this region. We have verified that this distance is sufficiently beyond the terminator to avoid scattered solar X-rays by examining wedges slightly farther beyond the terminator and determining that there is very little difference in the results when using these wedges.

Scattered solar X-rays from the sunlit lunar surface are an exceptionally bright diffuse source. Because of the ROSAT observation geometry, the Moon slid into the field of view and was therefore sampled with a point-spread function that varied from 10 arc sec to several arc minutes. This has the effect of overwhelming any signal from charge exchange from the lunar exosphere on the sunlit side for at least 0.2 lunar radii.

The antisolar wedge serves as a control wedge from which we expect very little SWCX emission because of the low solar wind flux there. The width, 38°, was chosen as the sum of the widths of the north and south wedges for ease of comparison assuming the expected symmetry around the subsolar point.

3. Interplanetary Solar Wind Conditions and Observations on the Dark Side

Here we discuss the solar wind conditions at the time of the ROSAT observations on 29 June 1990 from 02:10:52 to 03:05:43 UT. We compare the expected soft X-ray emission from the dark side of the Moon, that is, the emission from the magnetosheath as opposed to the lunar exosphere, to that expected on the basis on SWCX models. Note that, strictly speaking, due to the natural variability of the heavy ion component in

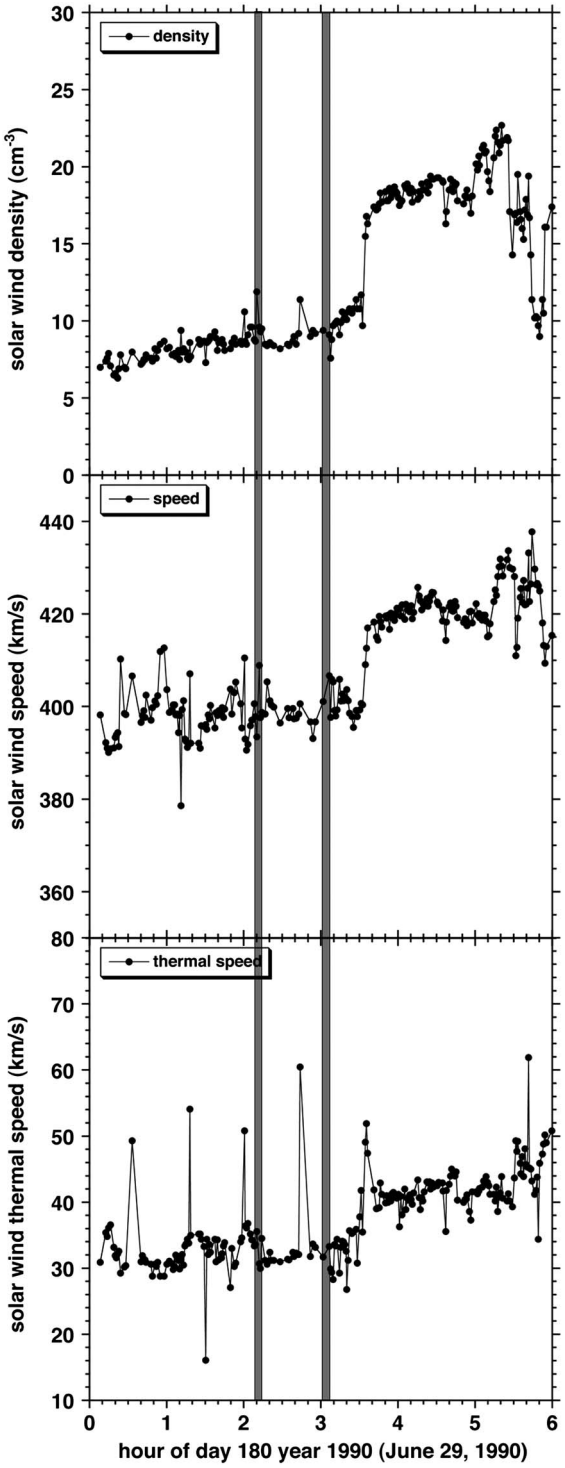

Figure 3. IMP-8 observations of the solar wind proton density, speed, and thermal speed during the first 6 h of 29 June 1990 (day 180) including the time of the ROSAT observation of the Moon. The time of the actual observation falls between the two vertical lines from 02:10:52 to 03:05:43 UT.

the solar wind, this comparison constitutes primarily a consistency check. However, because there is a reasonable correlation between the heavy ion flux and the proton flux in the solar wind [e.g., *Neugebauer et al.*, 2000, Figure 3], in practice this comparison tends to prove quite reliable.

Figure 3 shows Interplanetary Monitoring Platform-8 (IMP-8) observations of the solar wind proton density, speed, and thermal speed during the first 6 h of 29 June 1990. The two vertical lines indicate the period of the ROSAT observation. Note that over the period of observation, the solar wind flux was close to 3×10^8/cm^2/s, about an average solar wind flux [*Ruciński et al.*, 1996]. Over this time period, the interplanetary magnetic field was about 8 nT with a GSE x component of about −4 nT and y and z components of about 5 nT each.

There are frequently phase fronts oriented at various angles that can dramatically affect when solar wind structures are observed [e.g., *Collier et al.*, 1998; *Richardson and Paularena*, 2001; *Collier et al.*, 2005b]. At the time of the ROSAT observation of the Moon, the IMP-8 spacecraft was at approximately a GSE position of (25, 20, and 12) R_E. Also at this time, the Moon was at about GSE $y = 60\ R_E$, so given solar wind scale lengths that are typically ~ 10s of R_E (e.g., references in Table 1 of *Collier et al.*, 2000), the solar wind observations should be reliably representative of conditions at the Moon. Note that 20 to 30 min after the end of the ROSAT observation period, the solar wind flux increased to about 7×10^8/cm^2/s. Given the highly structured nature of the solar wind flow and the fact that the Moon and IMP-8 are separated by about 40 R_E in the direction perpendicular to the solar wind flow, it is possible given this spatial separation that the density enhancement IMP-8 observes 20 to 30 min after the ROSAT observation had already reached the Moon at the time of the observation. If this should be the case, then some or all of the ROSAT observation corresponds to this higher solar wind flux which would raise the expected soft X-ray emission from solar wind charge exchange by about a factor of 2.

Before discussing the limb brightening from the solar wind's interaction with the lunar exosphere, we will look at the soft X-ray flux observed by ROSAT on the dark side of the Moon's disk. These soft X-ray photons are produced by the solar wind's interaction with Earth's exosphere between the magnetopause and the Moon in the same way that solar wind charge exchange between solar wind protons and the terrestrial exosphere produces neutral

solar wind [e.g., *Collier et al.*, 2001]. Although the terrestrial exospheric density drops off rapidly with distance from Earth, at the nominal position of the magnetopause, there is still a substantial density ($\sim 10/\mathrm{cm}^3$) of exospheric hydrogen with which the solar wind can charge exchange [e.g., *Hodges*, 1994; *Østgaard et al.*, 2003] at (and beyond) the nominal magnetopause location. It is this emission that is observed when looking toward the dark side of the Moon's disk.

The SWCX emission originating in the magnetosheath is strongest on the dayside at the subsolar point of the magnetopause where the exospheric density is highest and the increase in solar wind density and temperature caused by the shock conspire to maximize emissions [*Carter and Sembay*, 2008]. ROSAT, however, because it always observes approximately perpendicular to the Sun-Earth line, is looking through the flank of the magnetosphere where SWCX emissions from the magnetosheath are much lower. Yet, as will be discussed, ROSAT clearly observes this magnetosheath signal.

Comparison of the off-Moon surface brightness of this observation with the cleaned ROSAT All-Sky Survey (RASS) surface brightness [*Snowden et al.*, 1997, 1998] in this direction indicates that the lunar observation has excess emission above the level of the soft X-ray background. This excess is a close match to the surface brightness observed from the dark side of the Moon and therefore originates in the near-Earth region, with charge exchange emission from the magnetosheath and exosphere being the only known source. Specifically, during the lunar observation, ROSAT detected 4195 counts/s/sr (where 1 count/s/sr ~ 0.145 ergs/cm^2/s/sr) in the 1/4 keV band toward the dark side of the Moon. The off-Moon rate was 13,350 counts/s/sr, yielding a difference between the on and off-Moon observations of $13,350 - 4195 = 9155$ counts/s/sr, which can be attributed to the cosmic X-ray background. The 1/4 keV band cleaned RASS rate in the direction of the lunar observation ($\alpha = 179.5°$, $\delta = -2.35°$) was 9450 counts/s/sr, only ~3% higher than the 9155 counts/s/sr inferred above. This provides a strong consistency check showing that the dark side emission originates foreground to the Moon and is not associated with the Moon.

Thus, with high confidence, we can conclude that the local emission between the Earth and the Moon due to solar wind charge exchange in the magnetosheath is about 4050 counts/s/sr, an average between the 4195 counts/s/sr inferred at the time of the observation and $13,350 - 9450 = 3900$ counts/s/sr inferred from the RASS observations. To convert this to an equivalent ROSAT LTE rate (count rate integrated over the entire detector) [*Cravens et al.*, 2001], we divide this number by 1753 (scaling from steradians to the PSPC field of view and then correcting for vignetting, the nonuniform sensitivity over the field of view), yielding 2.3 cts/s. Based on IMP-8 correlations with the observed ROSAT Long-Term Enhancement (LTE) rates, a ROSAT LTE rate of 0.36 cts/s corresponds to a solar wind flux of 10^8/cm^2/s so that 2.3 cts/s corresponds to a solar wind flux of 6.4×10^8/cm^2/s [e.g., see *Cravens et al.*, 2001]. This is higher, by about a factor of 2, than the observed solar wind flux over the observation time period. However, as discussed above, the solar wind flux did jump to about this level shortly after the observation which, although unlikely, could in principle be the source of the factor of 2 difference because the solar wind is so highly structured on these length scales. Considering this and the natural variability of the heavy ion component in the solar wind mentioned above, these results demonstrate consistency with expectations for the magnitude of the terrestrial exospheric component of the solar wind charge exchange soft X-ray emission. Note that it is not unusual for the observed SWCX soft X-ray emission to be higher than expected, particularly based on models [e.g., *Ishikawa et al.*, 2013].

Consequently, we turn our attention to an analysis of that component of the ROSAT soft X-ray observation of the Moon which is attributable to solar wind charge exchange *with the lunar exosphere* (as opposed to with the terrestrial exosphere). This component, because it results from an interaction with the lunar exosphere, manifests as limb brightening.

4. Quantitative Evaluation of Soft X-ray Flux as Limb Brightening

Figure 4 shows the observed ROSAT PSPC surface brightness in units of 10^{-6} counts/s/arc min^2 versus distance from the center of the Moon for the three wedges shown in Figure 2. Because the surface brightness is a measure of the intensity of the emission per solid angle, the plot naturally takes into account that the wedge area increases with radial distance and represents an average emission over the wedge segment.

The data reduction shown in Figure 4 and subsequent figures follows the general procedure described in *Snowden et al.* [1994]. However, the procedure was modified to create an image in a coordinate system fixed with respect to the Moon. Each photon ROSAT observed was first placed into a lunar-centric

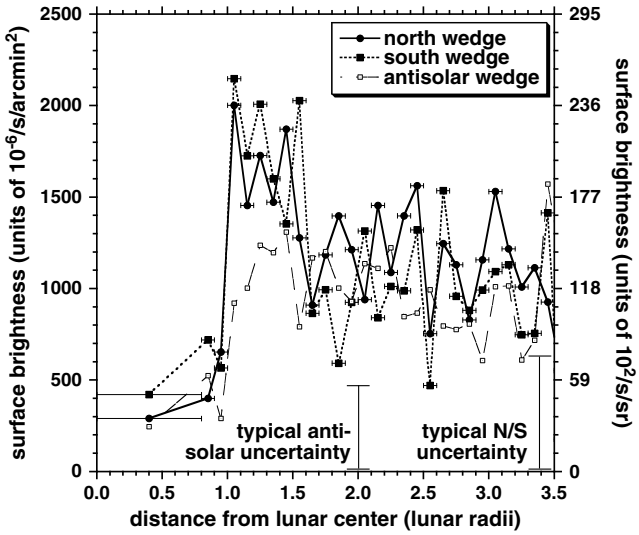

Figure 4. Plot showing as a function of distance from the center of the Moon the observed ROSAT surface brightness in the north (solid line) and south (short dashed line) 19° wedges as well as in the 38° antisunward (back) wedge (long dashed line). The north and south wedges run from 13° to 32° on the antisolar side of the terminator.

coordinate system. Then, a band-averaged exposure image was created by casting a detector map into the same lunar-centric coordinate system using the observation pointing aspect and orbit position data. The detector map was created from the ROSAT All-Sky Survey data which includes both vignetting and shadowing caused by the window support structure.

The instrumental particle background was modeled using the calibration of *Plucinsky et al.* [1993] and cast into an image in lunar-centric coordinates. The other backgrounds, namely, scattered solar X-rays and solar wind charge exchange from the magnetosheath and heliosphere, are approximately flat-field emission, so they only add a constant offset to the results. As discussed previously, solar wind charge exchange emission from the magnetosheath is likely responsible for the nonzero flux observed toward the dark side of the lunar disk.

The flux in each wedge was then determined by taking the summed counts (C), subtracting the modeled particle background counts (B), dividing by an exposure time (E), and finally multiplying by a scale factor that converts the results to physical units. The uncertainty in the modeled particle background is small compared to the statistical uncertainty in the observed counts, so the uncertainty in the flux is proportional to $\sqrt{C}$. Because the number of counts in each averaging bin does not change dramatically, neither do the statistical uncertainties, so, for legibility, we only show their typical value at the bottom of the plot.

Given the separation into north and south wedges, Figure 4 illustrates that both the north and south wedges show a dramatic increase in intensity relative to the antisolar wedge right on the limb of the Moon that decays over about 0.2 lunar radii. Outside of this radius on the edge of the Moon, the north, south, and back wedges show the same general trend in behavior. Thus, all three wedges show similar low intensities on the lunar disk attributed to SWCX near Earth and similar intensities attributed to the sum of this emission and the soft X-ray background well off the disk. However, the north and south wedges show an excess just beyond one lunar radius due to SWCX with the lunar exosphere.

Figure 5 shows the ROSAT data for the C-band (1/4 keV), where most of the solar wind charge exchange soft X-ray emission is expected to lie, with the north and south wedges combined to improve the contrast in the limb brightening. The limb brightening is indeed more obvious here and appears to be about 800×10^{-6} counts/s/arc min^2 (9450 counts/s/sr).

In principle, converting this limb-brightening enhancement of 9450 counts/s/sr into a flux in keV/cm^2/s/sr for comparison to the models requires knowing the soft X-ray spectrum and then folding that spectrum through the instrument response. However, in this case, the statistics do not allow such an approach. Instead we take 250 eV as an average-detected X-ray energy and use the instrument effective area of 220 cm^2 at 250 eV. With these assumptions, we get

$$\begin{aligned} 1\ \text{count/s/sr} &= 1\text{count/s/sr} \cdot 1.6 \times 10^{-12}\text{ergs/eV} \cdot 250\ \text{eV/count}\ /220\ \text{cm}^2 \\ &= 1.82 \times 10^{-12}\text{ergs/cm}^2\text{/sr/s}\ . \end{aligned} \tag{1}$$

Because the excess emission at the wedge segment closest to the Moon is about 9450 counts/s/sr, this yields a flux of 1.72×10^{-8} ergs/cm^2/s/sr or about 11 keV/cm^2/s/sr.

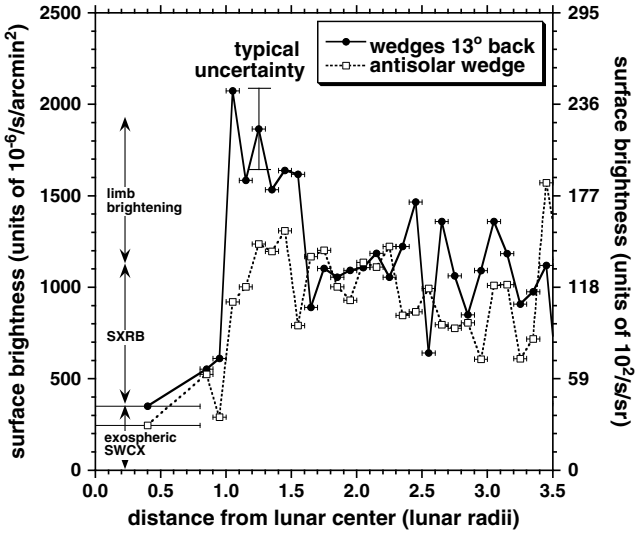

Figure 5. Same as Figure 4 but combining the north and south wedges for improved statistics. Here the typical uncertainty is shown on one point for clarity. Also, the Earth exospheric SWCX and soft X-ray background (SXRB) levels are shown along with the excess above these levels due to the limb brightening. Note that even though ROSAT is observing through the flank of the magnetosheath, the exospheric contribution is still a substantial fraction of the SXRB.

Also note that with reference to Figures 4 and 5, the increase in surface brightness of the antisolar wedge between the on-disk observations at less than one lunar radius and the off-disk observations at greater than one lunar radius is about a factor of 2 to 3. Because the on-disk observations only include solar wind charge exchange from the magnetosheath, whereas the off-disk observations include both the soft X-ray background and solar wind charge exchange from the magnetosheath, the strength of the magnetosheath emission during nominal solar wind conditions, like those during the time of the ROSAT observation of the Moon, is comparable to the soft X-ray background even when observing, like ROSAT, on the flank of the magnetosheath where emissions are much less intense than near the nose [e.g., *Collier et al.*, 2010]. As will be discussed later, no SWCX emission from the lunar exosphere contributes to the emission in the antisolar wedge because a negligible flux of solar wind makes it back there. Note that the on-disk emission 13° behind the terminator in Figure 5 is always higher than that in the antisolar wedge suggesting some contribution (< 50%) in these wedges due to SWCX with the lunar exosphere. Considering the detailed maps of the soft X-ray background generated by ROSAT during the all-sky survey, the sizeable SWCX emission from the magnetosheath apparent in Figure 5 even when observing through the flank clearly demonstrates the ability of a wide field-of-view imager to perform soft X-ray imaging of the magnetosheath.

5. Ion Access Beyond the Lunar Terminator—Observations

To compare this soft X-ray flux to that expected from solar wind charge exchange with the lunar exosphere, we need to determine the fraction of the solar wind that penetrates beyond 13° behind the terminator. That is, the solar wind flux, Φ_{sw}, that we need to consider here is not the nominal $3\times10^8/cm^2/s$ but rather the flux that arrives on the nightside 13° (and farther) behind the terminator.

Observationally, it is very clear that there is solar wind access beyond the terminator and even precipitation onto the surface. *Freeman and Ibrahim* [1975] report Apollo Lunar Surface Experiment Package (ALSEP) Suprathermal Ion Detector Experiment (SIDE) observations of ions having energies slightly lower than that of the solar wind occurring most frequently several days before local sunrise and several days after sunset. For example, the December 1969 observations started about 4.7 days (or 57.3°) before sunrise at the Apollo 12 ALSEP site [*Freeman*, 1972]. Because the mass analyzer data show that these ions have mass per unit charge lower than 10 amu/q, in contrast to events involving ions of lunar origin which have larger mass per unit charge values, they interpret the observations as due to singly ionized lighter ions or multiply ionized heavier ions. Thus, the logical candidate is solar wind ions that have been diverted to the nightside of the Moon. The observed ion events were bursty in character likely because the SIDE instruments have very narrow, 6° × 6°, fields of view, and as observations from both the Apollo 12 and Apollo 14 SIDE instruments show, the ion fluxes were directional [*Freeman*, 1972]. The observed flux is about 1% that of the solar wind [*Schneider and Freeman*, 1975].

SIDE sits on the lunar surface and so measures the flux of solar wind precipitating onto the surface. Because 1 day represents about 12.2° on the lunar surface, we assume based on the SIDE results that our north and south wedges in the ROSAT images which lie 13° off the terminator experience a precipitating solar wind

flux that is about 10^{-2} that of the nominal solar wind flux or $\Phi_{sw} = 3 \times 10^6/cm^2/s$. It is important to note that the flux of solar wind that contributes to charge exchange soft X-ray emission 13° off the terminator is significantly higher than this, because solar wind need not precipitate onto the surface to create soft X-rays but can be flowing away from the Moon.

Among more recent observations, the Japanese spacecraft SELENE (aka Kaguya) [*Kato et al.*, 2008; *Saito et al.*, 2010] has shown that, at 100 km altitude, solar wind protons can access regions as far antisunward as 150° solar zenith angle, that is, 60° beyond the terminator through a mechanism called "Type-I Entry" [*Nishino et al.*, 2009a]. In this process, the solar wind protons are accelerated by the charge separation electric field around the wake boundary. They enter the near-Moon wake perpendicular to the IMF as a result of their gyromotion.

Kaguya has also found solar wind proton entry into the deepest parts of the near-Moon wake via the "Type-II Entry." In this process, solar wind protons are scattered at the lunar dayside surface, picked up by the solar wind convection electric field, and transported into the deep wake region [*Nishino et al.*, 2009b].

Futaana et al. [2010] provided general confirmation of the Kaguya results. They also reported significant proton fluxes with energies slightly higher than the solar wind proton energy 50° behind the terminator entering the lunar wake parallel to the interplanetary magnetic field at an altitude of 100 km.

6. Ion Access Beyond the Lunar Terminator—Hybrid Model Results

The physics of solar wind ion and electron penetration into the lunar wake is at least qualitatively straightforward. The wake creates a downstream void in the solar wind flow. However, the electrons with a faster thermal speed than the protons lead the protons into the wake. This creates a charge separation, setting up a potential difference between the solar wind and the central wake [e.g., *Halekas et al.*, 2005]. In short, the larger thermal speed of the electrons allows them past the lunar limb to lead the slower ions into the wake. This, in turn, produces a charge separation which creates an electric field that slows the electrons but accelerates the ions into the wake [e.g., *Fatemi et al.*, 2012].

This process has been simulated by *Farrell et al.* [2008] who modeled solar wind filling in of the void region using a one-dimensional particle-in-cell code that does not require that the electron and ion densities be equal, that is, does not enforce charge neutrality.

However, analytically, the access of solar wind into the wake frequently is tackled with a fluid approach assuming isothermal electrons and cold ions and charge neutrality. *Halekas et al.* [2005] developed an analytic approach to ion filling of the lunar wake based on the work of *Samir et al.* [1983] which, given solar wind parameters such as electron temperature [*Newbury*, 1996], provides the proton density at various points in the wake. By assuming that the heavy ions are a small enough fraction of the overall solar wind that their presence does not affect quasi-neutrality (so that the proton density equals the electron density), the model can be expanded to include high charge heavy ions by invoking another fluid that must satisfy momentum and continuity in the presence of the electrostatic potential established by the protons and electrons. In the solar wind, the heavy ions have a mass to charge ratio of somewhere between about 2 and 10 [e.g., *Von Steiger and Zurbuchen*, 2006; *Galvin et al.*, 2009] with O^{+8} a major contributor to soft X-ray emission from SWCX because oxygen is fairly abundant in the solar wind [*Collier et al.*, 1996].

These analytic models, of course, are fluid treatments and ignore gyroradius effects that will be more important at larger mass per charges. Furthermore, one expects that models that ignore the magnetic field will be most applicable when the interplanetary magnetic field is at 90° with respect to the solar wind flow vector, that is, for flow along the field line.

However, simulations [e.g., *Nakagawa*, 2013] have shown that ions can enter the near-wake void along the magnetic field faster than predicted by analytical models. Furthermore, our three-dimensional hybrid simulations show that ions also can access the near-wake void perpendicular to the IMF because of their gyromotion.

Using a three-dimensional hybrid model [*Holmström et al.*, 2012; *Fatemi et al.*, 2012, 2013], we simulated the solar wind interaction with the Moon and, in particular, solar wind access into the void region given the measured solar wind conditions at the time of the ROSAT observations. Because the simulation treats ions

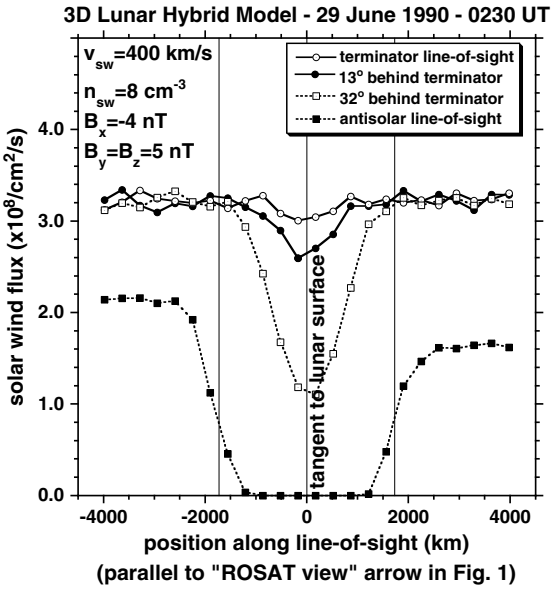

Figure 6. Results from the three-dimensional lunar hybrid model run with the solar wind parameters on 29 June 1990 during the time of the ROSAT observation. The four curves show the solar wind flux at various distances along a line of sight (see large arrow in Figure 1) that is tangent to the Moon at the terminator, 13° behind the terminator, 32° behind the terminator, and at the antisolar point. The position in kilometers along the line of sight is shown on the *x* axis of the plot measured from the tangent point of the Moon (at 0 km where the arrow in Figure 1 hits the Moon).

as individual particles, we can use the simulation results to evaluate the flux of solar wind that can access various positions along the ROSAT lines of sight.

Figure 6 shows the solar wind fluxes (i) along a terminator line of sight, (ii) 13° behind the terminator, (iii) 32° behind the terminator, and (iv) 90° behind the terminator (the antisolar point) where $y = 0$ is the tangent point to the lunar surface. The terminator line-of-sight flux is roughly constant and consistent with the undisturbed solar wind flux. At 13° behind the terminator, the front edge of the north/south wedge, although there is some slight decrease in solar wind flux behind the Moon, there is always a substantial flux, about $2.7 \times 10^8/\text{cm}^2/\text{s}$. At 32° behind the terminator, the back end of the north/south wedge, the solar wind flux is lower but still about $1.2 \times 10^8/\text{cm}^2/\text{s}$. Note that not included in this simulation is the suprathermal part of the solar wind distribution [e.g., *Collier*, 1993] which has easier access to the near lunar deep wake because of their larger gyroradii [*Dhanya et al.*, 2013].

The asymmetry in the antisolar line of sight solar wind flux levels far from the Moon, about $2.2 \times 10^8/\text{cm}^2/\text{s}$ at negative *y* and about $1.6 \times 10^8/\text{cm}^2/\text{s}$ at positive *y* likely results from the orientation of the interplanetary magnetic field during the time of the ROSAT observation, approximately in the *x*-*y* plane along the nominal Parker spiral direction. Particles, because of their gyromotion, more easily fill void regions by moving along the field lines than by moving across the field lines. Consequently, the Parker-like IMF configuration allows more rapid filling on the negative GSE-*y* side which can be immediately accessed by upstream protons moving in the negative GSE-*x* direction.

It is important to note that the solar wind flux close to the surface (as shown simulated in Figure 6) is substantially higher than the flux that precipitates onto the surface. Precipitating flux must have a velocity toward the lunar surface, and the 1% of the solar wind flux SIDE measured [*Schneider and Freeman*, 1975] on the nightside within a few days of the dawn and dusk terminators represents the precipitating flux because SIDE sits on the lunar surface. The hybrid simulations show a flux onto the lunar surface of about 10^{-3}–10^{-1} the ambient solar wind flux depending on angle behind the terminator, roughly consistent with the SIDE observations as well as the two-dimensional simulations of ambipolar expansion presented in *Farrell et al.* [2008].

As a general comment on the simulation results, during conditions when the IMF is perpendicular to the solar wind flow, protons access the void region more readily because their higher charge to mass ratio allows the electric field to accelerate them more effectively into the void region. Although the hybrid simulation enforces charge neutrality explicitly [*Holmström et al.*, 2012; *Fatemi et al.*, 2012, 2013], the charge separation electric field manifests as an ambipolar electric field driven by the pressure gradient that produces the same physical effect. In contrast, during periods when the IMF is parallel to the solar wind flow, the simulations show that the ion gyroradius is the dominant factor with the heavier ions entering the void region more easily than the protons because they have larger gyroradii.

Using the three-dimensional hybrid model under conditions when the IMF is precisely parallel to the solar wind flow as well as approximately perpendicular to the solar wind flow, the solar wind appears to penetrate at least as far as 30° beyond the terminator in either IMF configuration. Indeed, such a conclusion appears to be supported by the (two-dimensional) simulations of *Nakagawa* [2013, see, e.g., Figure 1] as well.

Strong lunar magnetic anomalies near the ROSAT line of sight could effectively deflect solar wind ions shielding the regions close to the lunar surface where exospheric densities are greatest and lowering the expected soft X-ray emission [e.g., *Mitchell et al.*, 2008]. However, there do not appear to be any significant anomalies in the relevant regions.

Also, note that the simulation confirms that the antisolar wedge is a good control line of sight because no detectable solar wind flux arrives directly behind and tangent to the Moon on this line of sight so there is no predicted emission from SWCX here. This is not unexpected [see, for example, *Holmström et al.*, 2012, Figure 8; *Fatemi et al.*, 2012].

In summary, although 13°–32° beyond the terminator the solar wind flux within 100 km of the lunar surface is somewhat lower than that in the undisturbed solar wind, a significant flux can access this region, $\sim 10^8/\mathrm{cm}^2/\mathrm{s}$ based on the hybrid model results. This is in contrast to the flux of precipitating solar wind which is much lower, $\sim 10^6/\mathrm{cm}^2/\mathrm{s}$.

7. Soft X-rays From Surface Impact

In principle, heavy high charge state solar wind ions that hit the lunar surface will charge exchange with surface constituents resulting in soft X-ray and EUV emission [e.g., *Kallio et al.*, 2008]. Both the pronounced limb brightening and the calculation above showing that the observed emission on the disk is consistent with solar wind charge exchange with the terrestrial exosphere suggest that this is not a significant effect for our purposes here.

However, here we attempt to estimate based on available data the soft X-ray flux generated from solar wind heavy ions precipitating onto the lunar surface into the 19° wedge of radial extent 0.1 R_{Moon} located 13° behind the terminator where we observe the limb brightening. We will then compare this flux to the observed limb brightening to determine the degree to which this process contributes to the soft X-ray emission from this region.

We assume, as discussed in the previous section, that 1% of the solar wind flux precipitates 13° behind the terminator so that

$$\begin{aligned} \Phi_{\mathrm{sw\ wake}} &= 0.01 \cdot 3 \times 10^8/\mathrm{cm}^2/\mathrm{s}, \\ &= 3 \times 10^6/\mathrm{cm}^2/\mathrm{s}\ , \end{aligned} \tag{2}$$

and that 0.1% of this flux is solar wind heavy ions or

$$\begin{aligned} \Phi_{\mathrm{heavy\ wake}} &= 10^{-3} \cdot 3 \times 10^6/\mathrm{cm}^2/\mathrm{s}, \\ &= 3 \times 10^3/\mathrm{cm}^2/\mathrm{s}\ . \end{aligned} \tag{3}$$

We are observing on the surface of the Moon a 0.1 R_{Moon} by 19° angular segment. Therefore, the angular range, θ, on the lunar surface covered by the 0.1 R_{Moon} projected distance is given by

$$0.1\ R_{\mathrm{Moon}} = 1\ \mathrm{R}_{\mathrm{Moon}} \cdot (1 - \cos\theta), \tag{4}$$

or $\theta = 25.8°$. Thus, we are observing approximately

$$\begin{aligned} \mathrm{d}\Omega &= 19° \cdot \frac{\pi}{180°}\ \cdot\ 25.8° \cdot \frac{\pi}{180°} \\ &= 0.15\ \mathrm{sr}\ , \end{aligned} \tag{5}$$

of the 4π sr lunar surface. The area, A, thus observed is

$$\begin{aligned} A &= \mathrm{R}^2_{\mathrm{Moon}} \mathrm{d}\Omega, \\ &= 4.5 \times 10^{15}\ \mathrm{cm}^2\ . \end{aligned} \tag{6}$$

This means that the rate, R, of solar wind heavy ion impingement onto the surface here is

$$\begin{aligned} R &= 3 \times 10^3/\mathrm{cm}^2/\mathrm{s} \cdot 4.5 \times 10^{15}\ \mathrm{cm}^2, \\ &= 1.4 \times 10^{19}\ \mathrm{s}^{-1}. \end{aligned} \tag{7}$$

Based on *Ninomiya et al.* [1998, Figure 1], which is for Ar impinging on an amorphous carbon target with velocities from 0.9 keV/nucleon (415 km/s) to 3.3 keV/nucleon (795 km/s), standard solar wind speeds, and using the Ar charge states in the solar wind of 8–10, somewhere around 5×10^{-5} soft X-ray photons per ion are created. Assuming that this is typical of the solar wind heavy ion soft X-ray production that results from hitting the lunar regolith, the photons created per second, R_γ, in this 0.1 R_{Moon} by 19° region is

$$\begin{aligned} R_\gamma &= 1.4 \times 10^{19}/\mathrm{s} \cdot 5 \times 10^{-5} \text{ photons}, \\ &= 7 \times 10^{14} \text{ photons/s}. \end{aligned} \tag{8}$$

ROSAT is observing at Earth at a distance of 60 R_E, so this appears as a point source with the area flux decreasing inversely with the square of the radius at which the emission is observed. Also, the emission from the lunar surface is assumed to occur uniformly over a half sphere or 2π steradians. Consequently, the total photon area flux, F, observed at Earth is

$$\begin{aligned} F &= 7 \times 10^{14} \text{ photons/s}/2\pi/(60 \cdot 6371 \times 10^5 \text{ cm})^2, \\ &= 7.6 \times 10^{-8} \text{ photons/s/cm}^2. \end{aligned} \tag{9}$$

Because these photons are observed coming from a 19°×0.1 R_{Moon} segment of the lunar disk, and a lunar radius is about 0.25° on the sky, the total solid angle the Moon covers on the sky is about 6×10^{-5} sr ($= \pi(0.25° \cdot \pi/180°)^2$). The observed wedge has an area relative to the lunar disk of $19°/360° \cdot (1^2 - 0.9^2) = 0.01$ so that the solid angle of the wedge is $0.01 \cdot 6 \times 10^{-5}$ sr $= 6 \times 10^{-7}$ sr.

Therefore, the observed photon intensity, Φ_γ, is

$$\begin{aligned} \Phi_\gamma &= 7.6 \times 10^{-8} \text{ photons/s/cm}^2/6 \times 10^{-7} \text{ sr}, \\ &= 0.13 \text{ photons/s/cm}^2/\text{sr}. \end{aligned} \tag{10}$$

If we take each photon to be 250 eV, a conservative assumption, the predicted soft X-ray intensity, Φ, due to high charge state solar wind heavy ions hitting the surface is about

$$\begin{aligned} \Phi &= 0.25 \text{ keV} \cdot 0.13/\text{s/cm}^2/\text{sr}, \\ &= 3.2 \times 10^{-2} \text{ keV/s/cm}^2/\text{sr}, \end{aligned} \tag{11}$$

so the observed limb brightening is about 2 orders of magnitude greater than the expected soft X-ray flux due to solar wind heavy ions hitting the lunar surface.

8. Exospheric Density Estimate From ROSAT Soft X-ray Observations on the Limb

With some assumptions, we can use the observed limb-brightening soft X-ray flux to estimate the associated lunar exospheric surface density. In an approach similar to that of *Collier and Stubbs* [2009], we assume we are viewing the Moon from the side and take a to be the radius of the Moon, 1738 km. We wish to evaluate the column density, C,

$$C = \int n \cdot \mathrm{d}l, \tag{12}$$

where l is the distance along the line of sight measured from the tangent point. We assume that the exospheric density drops off exponentially with scale height λ such that $n = n_0\, e^{-h/\lambda}$ where n_0 is the surface density and h is the height above the surface. Thus,

$$h = \sqrt{a^2 + l^2} - a. \tag{13}$$

Typically, the exosphere scale height is much less than a lunar radius, $a = 1738$ km. Consequently, the l values contributing significantly to the integral C above will also be much less than a lunar radius. Therefore, we take $l \ll a$ and approximate

$$\begin{aligned} h &= a \cdot \sqrt{1 + l^2/a^2} - a, \\ &\approx a \left[1 + \frac{l^2}{2a^2}\right] - a, \\ &= \frac{l^2}{2a}. \end{aligned} \tag{14}$$

Thus, we can approximate the integral as

$$\int n \cdot \mathrm{d}l = \int_{-\infty}^{+\infty} n_0 \, e^{-h/\lambda} \, \mathrm{d}l, \approx \int_{-\infty}^{+\infty} n_0 \, e^{-l^2/2a\lambda} \, \mathrm{d}l. \tag{15}$$

Noting that the expression for a normalized one-dimensional Gaussian is

$$\frac{1}{\sqrt{2\pi}\sigma} \int_{-\infty}^{+\infty} e^{-x^2/2\sigma^2} \, \mathrm{d}x = 1, \tag{16}$$

and identifying σ^2 with $a\lambda$, the expression (15) becomes

$$\int n \cdot \mathrm{d}l = \int_{-\infty}^{+\infty} n_0 \, e^{-l^2/2a\lambda} \, \mathrm{d}l, = n_0 \sqrt{2\pi a\lambda}. \tag{17}$$

So the limb viewing enhances the column density scaling estimate of $n_0\lambda$ by a factor of $\sqrt{2\pi a/\lambda}$ which for $a = 1738$ km and $\lambda = 100$ km is ~10.

The expected X-ray intensity Φ due to solar wind charge exchange along a given line of sight is given by

$$4\pi\,\Phi = \alpha\Phi_{sw} \int n \, \mathrm{d}l, \tag{18}$$

where Φ_{sw} is the solar wind flux and α is a factor that represents the possible transitions and their weighted cross sections [e.g., *Robertson et al.*, 2009; *Robertson et al.*, 2006]. The value of α that we will use here is 6×10^{-16} eV cm^2 which corresponds to a target species of most gases [*Pepino et al.*, 2004; *Greenwood et al.*, 2000].

Using expression (17), equation (18) becomes

$$4\pi\,\Phi = \alpha\Phi_{sw} n_0 \sqrt{2\pi a\lambda}. \tag{19}$$

As discussed earlier, we take Φ_{sw} to be 2×10^8/cm^2/s. Using the observed limb brightened increase in the soft X-ray emission of 11 keV/cm^2/s/sr and a nominal $\lambda = 100$ km, we can estimate the density as

$$\begin{aligned} n_0 &= \frac{4\pi\,\Phi}{\alpha\Phi_{sw}\sqrt{2\pi a\lambda}} \\ &= \frac{4\pi \text{ sr} \cdot 11 \text{ keV/cm}^2\text{/s/sr}}{6\times10^{-19} \text{ keV cm}^2 \cdot 2\times10^8\text{/cm}^2\text{/s} \cdot \sqrt{2\pi \cdot 1738\times10^5 \text{ cm} \cdot 100\times10^5 \text{ cm}}} \\ &= 10^4 \text{ cm}^{-3}. \end{aligned} \tag{20}$$

This is a reasonable lunar exospheric density [e.g., *Stern*, 1999] and suggests that not only the qualitative character, that is, limb brightening, but also the quantitative character of this signal is consistent with being due to solar wind charge exchange with the lunar exosphere.

9. Comparison With Models

These ROSAT observations of SWCX with the lunar exosphere can be compared to predictions using lunar exospheric models. Among these are the Lunar Exosphere Simulator model [*Hodges*, 2011] which will use the upcoming Lunar Atmosphere and Dust Environment Explorer (LADEE) data to calibrate its surface physics parameters [*Elphic et al.*, 2011] and the model of *Sarantos et al.* [2012].

The *Sarantos et al.* [2012] model simulated the production and loss of exospheric O, Si, and other metallic species assuming that the operative loss processes for the lunar exosphere are ballistic escape, photoionization, and recycling at the surface. The model was an extension of an earlier model [*Sarantos et al.*, 2010] of exospheric particle transport that successfully described the lunar Na atmosphere and was based on analytically computing the phase space distribution function of ejecta in gravity fields [*Hartle*, 1971]. That model tracked the ballistic trajectories until particles escaped or returned to the surface. Atoms returning to the

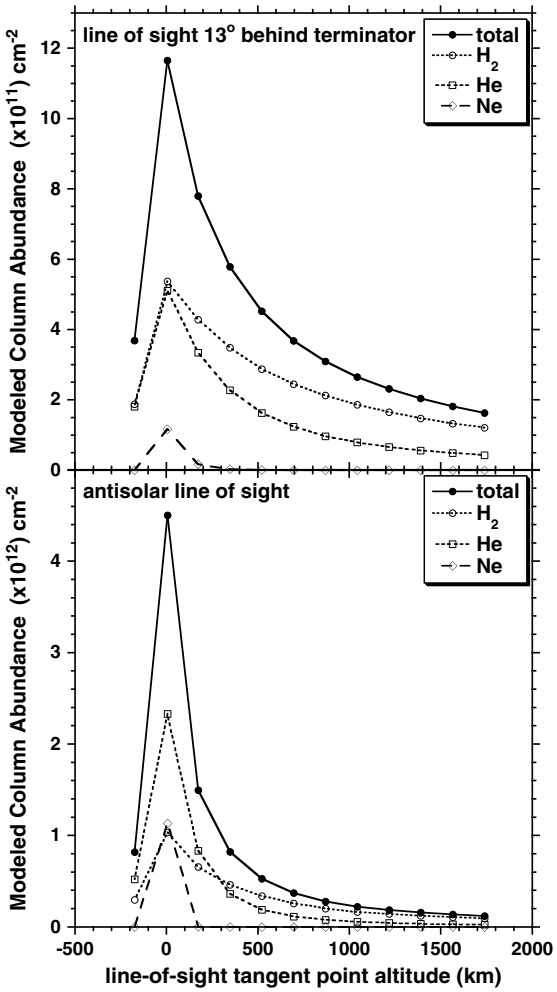

Figure 7. The column densities (i.e., the line integral of the density: $\int n\,dl$) for various species in the lunar exosphere using the model of *Sarantos et al.* [2012] extended to include volatiles. Plotted on the *x* axis is the tangent point altitude so that 0 km shows the effect of limb brightening. (top) The column densities relevant to the ROSAT observations, i.e., 13° behind the terminator and (bottom) the column densities along the antisolar line of sight (for comparison). Because a negligible flux of solar wind penetrates this far behind the Moon, very little SWCX soft X-ray emission occurs due to the lunar exosphere along this line of sight. In both plots the solid line is the total column abundance. Note the difference in scale on the *y* axis of the two plots.

surface were assumed to be adsorbed and were not rereleased so that the primary loss mechanisms were ballistic escape and hitting the surface. The assumption of perfect sticking is valid for refractories. Thus, the model as published considered only regolith-derived atoms in the lunar exosphere, that is, those originating from solar photons, solar wind ions, and micrometeoroids hitting the lunar surface. However, here we compare to an extension of the published model that includes volatiles.

Volatiles are not adsorbed when they recycle. Therefore, to simulate the concentration and local time distribution of key volatile constituents, we used a test particle Monte Carlo approach [e.g., *Killen et al.*, 2012]. We assumed that test particles representing H_2, He, and Ne thermally desorb from the soil and accommodate to the local surface temperature upon return to the surface (H is only a weak contributor). These three species do not stick even at the coldest temperatures of the lunar nightside surface. By reintroducing these particles into the simulation and counting them until photodissociation and photoionization eliminate them, much higher exospheric densities are achieved. As in *Sarantos et al.* [2010, 2012], the model requires an estimate of production flux of particles of a given species to evaluate densities. For this simulation, the subsolar production rates were assumed to be 7.5×10^7 H_2 atoms/cm^2/s, 9×10^6 He atoms/cm^2/s, and 6×10^3 Ne atoms/cm^2/s. These rates correspond to the solar wind influx of 3×10^8 protons/cm^2/s for this interval and assume 50% conversion of the incident solar wind to H_2 in the lunar soil, 3% abundance of He in the solar wind, and a thousand times less Ne than He in the solar wind.

Figure 7 shows the column density for H_2, He, and Ne in the lunar exosphere using the Monte Carlo model for lines of sight 13° behind the terminator (Figure 7, top) and toward the antisolar direction (Figure 7, bottom). The plot is for the north, but the model is symmetric with respect to the subsolar point, so the results for the south are identical. Plotted on the *y* axis is the integrated density, the column abundance, for each species in cm^{-2}. Plotted on the *x* axis in each panel is the tangent point of the line of sight so that, for example, the peak at 0 km corresponds to limb brightening. In the wedge 13° behind the terminator, the predicted column abundance at the limb is $\sim 1.2 \times 10^{12}$/cm^2 from these three species which is to be contrasted with the total column density of 5×10^{10}/cm^2 from the refractories studied by *Sarantos et al.* [2012]. The antisolar region model predictions are slightly higher at the limb but drop off faster with tangent height because of the shorter scale heights of neutrals in this region. Therefore, the wedges observed by ROSAT behind the terminator are dominated by H_2, He, and Ne, and potentially by Ar, which was not modeled. Note that the magnitude of the dropoff from the peak on the limb is an indicator of the mass of the dominant species in the exosphere at this subsolar longitude.

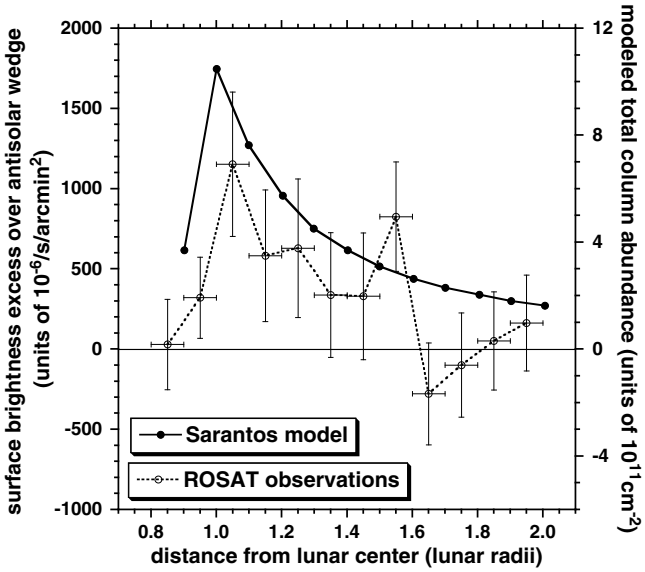

Figure 8. A comparison between the excess surface brightness in the 13° wedge over that in the antisolar wedge, the SWCX component, and the modeled total column abundance from the *Sarantos et al.* [2012] model extended to include volatiles as a function of distance from the lunar center. The enhancement profile is roughly consistent with that predicted by the Sarantos et al. model, and noting that the solar wind flux is relatively constant with distance from the Moon at this location, is also consistent with the expected contribution of SWCX soft X-ray emission from the solar wind interaction with the lunar exosphere.

The total column density, $\int n \cdot dl$, predicted by the model in the wake 13° behind the terminator is about 1.2×10^{12} cm^{-2}. Using the relationship

$$4\pi\,\Phi = \alpha\Phi_{sw} \int n\,dl, \tag{21}$$

with $\alpha = 6 \times 10^{-16}$ eV cm^2 and $\Phi_{sw} = 2 \times 10^8$/cm^2/s based on the 3-D hybrid code results, we get

$$\Phi = \frac{6 \times 10^{-16}\ \text{eV cm}^2 \cdot 2 \times 10^8/\text{cm}^2/\text{s} \cdot 1.2 \times 10^{12}\ \text{cm}^{-2}}{4\pi\ \text{sr}} = 11\ \text{keV/cm}^2/\text{s/sr}. \tag{22}$$

Thus, the flux predicted by the models is ~11 keV/cm^2/s/sr which is also the flux observed by ROSAT.

The observed and modeled values are in reasonable agreement considering the uncertainty in the H_2 column abundance as well as the uncertainty in the appropriate value of Φ_{sw}; for example, if the solar wind flux is actually 7×10^8/cm^2/s as discussed in section 3, then the predicted flux more than doubles. Additionally, it is not unusual for models to underestimate the observed SWCX emission [e.g., *Koutroumpa et al.*, 2009].

Figure 8 compares the difference between the surface brightness observed by ROSAT in the wedges 13° back from the terminator and that observed in the antisolar wedge, as shown in Figure 5 (open circles and dashed line) with the predictions of the Sarantos model shown in Figure 7 (solid circles and solid lines). It is expected that the solar wind flux, based on hybrid model results shown in Figure 6, remains reasonably close to its undisturbed flux level so that one can directly compare the observed excess soft X-ray surface brightness to the modeled total column abundance. Although the uncertainties for the ROSAT observations are relatively large, excess surface brightness above that observed in the antisolar wedge exists up to about 1.3 lunar radii. Furthermore, the observed excess surface brightness profile is consistent with the predictions of the Sarantos model shown in Figure 8 on the right hand *y* axis.

Note that, with regard to both Figures 7 and 8, it is the case that the line of sight at $x = -170$ km (0.9 lunar radii) is occulted by the surface of the Moon, so the length of the line of sight and the corresponding soft X-ray intensity drop off significantly. Because the models do provide predictions at this location, we have included line-of-sight tangent points below 0 km on these plots.

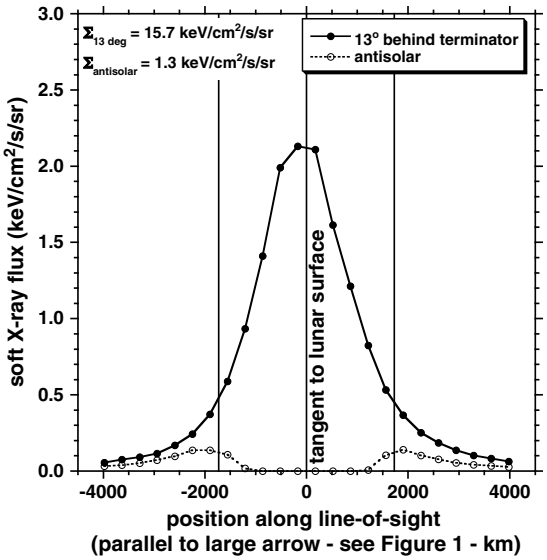

Figure 9. A convolution of the hybrid model results shown in Figure 6 and the Sarantos model densities along the line of sight. The *y* axis indicates the soft X-ray flux in keV/cm^2/s/sr that originates in a path length of 346 km centered on each point for a line of sight 13° behind the terminator (solid line and solid circles). The sum of the contribution at each point along the line of sight is the total soft X-ray flux. The total for the line of sight 13° behind the terminator is 15.7 keV/cm^2/s/sr while the total for the antisolar line of sight is 1.3 keV/cm^2/s/sr. This is consistent with the observed ROSAT soft X-ray flux of 11 keV/cm^2/s/sr.

The magnitude of the dropoff from the peak on the limb is an indicator of the mass of the dominant species in the exosphere at this subsolar longitude. So observations with less uncertainty (e.g., taken over a longer period) would also provide a diagnostic of exospheric composition.

It is possible that the gradual soft X-ray flux dropoff seen in Figure 5 may also be due to the presence of reflected neutral atoms off the lunar surface. *Wieser et al.* [2009] using measurements from the Sub-keV Atom Reflecting Analyzer instrument on the Indian Chandrayaan-1 spacecraft in lunar orbit found that up to 20% of the solar wind protons that hit the lunar surface are reflected back off the regolith as neutral hydrogen atoms. The observed reflected hydrogen has a wide energy distribution with roughly half the energy of the impinging solar wind, so they are escaping atoms on ballistic trajectories. Consequently, these atoms will form a neutral population around the Moon with very large scale lengths with which the incoming solar wind will charge exchange. Note also that because the neutral density increases in proportion to the solar wind density, the soft X-ray flux from this "self-emission" process in which the solar wind charge exchanges with itself will increase nonlinearly, with the square of the solar wind density.

Although the above calculation serves as a good estimate of the predicted emission from the solar wind hybrid and lunar exosphere models, in actuality, the results of Figure 6 should be multiplied by the density at each point along the line of sight and integrated along the entire line of sight to calculate the expected emission. So Figure 9 shows at each point along the line of sight 13° behind the terminator and antisolar the soft X-ray flux from that point, $\alpha/4\pi \cdot \Phi_{sw} \cdot n \cdot \Delta l$, in keV/cm^2/s/sr where as discussed earlier $\alpha = 6 \times 10^{-19}$ keV cm^2 while Φ_{sw} and n are the solar wind flux and exospheric density, respectively, at a given point along the line of sight. The value of Δl is determined by the spacing of the points, $\Delta l = 346 \times 10^5$ cm. The sum of all the data points is the total emission along the line of sight.

As indicated in Figure 9 (top, left), the sum of the intensity along the line of sight 13° behind the terminator is 15.7 keV/cm^2/s/sr, close to the estimated value of 11 keV/cm^2/s/sr given by equation (22) and observed by ROSAT. As expected, the estimate for the front of the wedge, 13° behind the terminator, is higher than the value inferred by using a typical solar wind flux across the wedge, as was done in equation (22). Conversely, the sum of the intensity along the antisolar line of sight is 1.3 keV/cm^2/s/sr, less than a tenth of the predicted emission 13° behind the terminator and consistent with the ROSAT observation in Figure 5 that shows no observable limb brightening in the antisolar wedge.

10. Discussion

As is apparent from the results presented here, soft X-ray imaging off the limb of the Moon can provide diagnostics about the source and properties of the lunar exosphere. For example, the dominant contributors to the exospheric column density, H_2, He, and Ne, are species known to be controlled by the solar wind influx. Recently, the relationship between the solar wind flux and the lunar exosphere was observed directly. The Lyman Alpha Mapping Project (LAMP) ultraviolet spectrograph on NASA's Lunar Reconnaissance Orbiter (LRO) Mission made observations between 29 December 2011 and 26 January 2012 of the lunar helium exosphere which originates from solar wind ions that become neutralized and thermalized through

interaction with the lunar surface [*Feldman et al.*, 2012]. LRO/LAMP found that the surface He density exhibited day-to-day variations responding to variations in the solar wind alpha particle flux. Thus, the X-ray technique can be used to monitor the fluctuation of the lunar exosphere with variations in the solar wind flux on a continual basis.

However, the Moon is only in the solar wind about two thirds or so of the time; the remainder it spends in the terrestrial magnetotail where it is largely shielded from the solar wind. There are high charge state solar wind ions in the magnetotail in its plasma sheet [e.g., *Christon et al.*, 1994; *Kremser et al.*, 1987]. However, the plasma sheet occupies a relatively small portion of the overall magnetotail cross section, which consists of mostly the very low density lobes, and the densities of plasma sheet solar wind ions are significantly lower than those in the solar wind [e.g., *Lui*, 1987]. So the expected SWCX soft X-ray emission would also be correspondingly lower. Consequently, another method to study the behavior of the lunar exosphere is to examine the modulation of the soft X-ray signal as the Moon moves in and out of the terrestrial magnetotail. This approach would be similar to that used by *Potter et al.* [2000] who measured sodium emission [e.g., *Tenishev et al.*, 2013] above the lunar equator and showed that the passage of the Moon through the Earth's magnetotail caused the sodium density to fall. This suggested that the solar wind plays a role in the production of lunar sodium.

In the case of SWCX soft X-ray emission, observations of the Moon from low Earth orbit while the Moon is in the magnetotail would be overwhelmed by scattered solar X-rays from the lunar surface. This is because full moon periods correspond to times when the Moon is in the magnetotail. Consequently, this type of measurement would be best made on a mission that has a large enough apogee to at least exit the magnetosphere [e.g., *Branduardi-Raymont et al.*, 2012; *Sembay et al.*, 2012], and wide field-of-view soft X-ray cameras for this and similar applications have been developed [e.g., *Collier et al.*, 2012]. Of course, such a mission would also image the much stronger magnetosheath soft X-ray emission [e.g., *Collier et al.*, 2010].

11. Conclusions

The ROSAT remote observations of solar wind charge exchange soft X-ray emission with the lunar exosphere provide substantial experimental input for models of the lunar exosphere and of solar wind access into the near-Moon wake. Although certain species in the lunar exosphere, notably Na, may be observed remotely, the relative insensitivity of the charge exchange mechanism to the target species means that soft X-ray emission provides a diagnostic for the total exospheric density and not just the density of a particular species. For example, using this type of measurement, we could constrain polar cold trapping efficiencies over the lunar north and south poles. Of course, the capability to make these lunar measurements remotely, from even low Earth orbit, reduces both cost and complexity while providing a larger-scale picture than is possible with in situ measurements.

Clearly, a dedicated lunar soft X-ray SWCX mission, rather than a single observation from an astrophysics telescope, would provide much needed data on the properties of the solar wind-lunar interaction and the lunar exosphere.

Acknowledgments

This material is based upon work supported by (1) the National Aeronautics and Space Administration under grant LSSO06-0032 issued through the Science Mission Directorate's Planetary Science Division, (2) the Dynamic Response of the Environment At the Moon (DREAM) NASA Lunar Science Institute team, and (3) the NASA Solar System Exploration Research Virtual Institute (SSERVI), Dynamic Response of the Environment at Asteroids, the Moon, and moons of Mars (DREAM2) team. This paper may be tracked via SSERVI-2014-098. We have made use of the ROSAT Data Archive of the Max-Planck-Institut für extraterrestrische Physik (MPE) at Garching, Germany. Thanks to Robert E. McGuire for OMNI, CDAWeb, and Satellite Situation Center (SSC) Web data as well as to Leonard Garcia for SSC support. Special thanks to John Cooper and John Keller for pointing us to useful references. Part of this work was performed while the primary author and many of the coauthors were attending the International Space Science Institute (ISSI) workshop on solar wind charge exchange in January 2013 in Bern, Switzerland. We gratefully acknowledge ISSI's hospitality. Also, part of this work was performed while the primary author was visiting the Swedish Institute of Space Physics (IRF) in Kiruna, Sweden, on an 89 day Science and Exploration Division (SED) Fellowship in spring 2013 supported jointly by Goddard Space Flight Center and the Swedish Institute of Space Physics. He gratefully acknowledges IRF's hospitality and SED's generosity. The computations were performed on resources provided by the Swedish National Infrastructure for Computing (SNIC) at the High Performance Computing Center North (HPC2N).

References

Bhardwaj, A., et al. (2007), X-rays from solar system objects, *Planet. Space Sci.*, *55*(9), 1135–1189, doi:10.1016/j.pss.2006.11.009.

Branduardi-Raymont, G., et al. (2012), AXIOM: Advanced X-ray imaging of the magnetosphere, *Exp. Astron.*, *33*(2), 403–443, doi:10.1007/s10686-011-9239-0.

Carter, J. A., and S. Sembay (2008), Identifying XMM-Newton observations affected by solar wind charge exchange: Part I, *Astron. Astrophys.*, *489*(2), 837–848.

Christon, S. P., D. C. Hamilton, G. Gloeckler, T. E. Eastman, and F. M. Ipavich (1994), High charge state carbon and oxygen ions in Earth's equatorial quasi-trapping region, *J. Geophys. Res.*, *99*, 13,465–13,488.

Collier, M. R. (1993), On generating kappa-like distribution functions using velocity space Lévy flights, *Geophys. Res. Lett.*, *20*, 1531–1534.

Collier, M. R., D. C. Hamilton, G. Gloeckler, P. Bochsler, and R. B. Sheldon (1996), Neon-20, oxygen-16, and helium-4 densities, temperatures, and suprathermal tails in the solar wind determined with WIND/MASS, *Geophys. Res. Lett.*, *23*, 1191–1194, doi:10.1029/96GL00621.

Collier, M. R., J. A. Slavin, R. P. Lepping, A. Szabo, and K. Ogilvie (1998), Timing accuracy for the simple planar propagation of magnetic field structures in the solar wind, *Geophys. Res. Lett.*, *25*, 2509–2512.

Collier, M. R., A. Szabo, J. A. Slavin, and R. P. Lepping (2000), IMF length scales and predictability: The two length scale medium, *Int. J. Geomag. Aeron.*, *2*(1), 3–16.

Collier, M. R., et al. (2001), Observations of neutral atoms from the solar wind, *J. Geophys. Res.*, *106*, 24,893–24,906.

Collier, M. R., T. E. Moore, M. C. Fok, B. Pilkerton, S. Boardsen, and H. Khan (2005a), Low-energy neutral atom signatures of magnetopause motion in response to southward B_z, *J. Geophys. Res.*, *110*(A2), A02102, doi:10.1029/2004JA010626.

Collier, M. R., T. E. Moore, S. L. Snowden, and K. D. Kuntz (2005b), One-up on L1: Can X-rays provide longer advanced warning of solar wind flux enhancements than upstream monitors?, *Adv. Space Res.*, *35*, 2157–2161, doi:10.1016/j.asr.2005.02.035.
Collier, M. R., and T. J. Stubbs (2009), Neutral solar wind generated by lunar exospheric dust at the terminator, *J. Geophys. Res.*, *114*, A01104, doi:10.1029/2008JA013716.
Collier, M. R., D. G. Sibeck, T. E. Cravens, I. P. Robertson, and N. Omidi (2010), Astrophysics noise: A space weather signal, *Eos Trans. AGU*, *91*(24), 213–214.
Collier, M. R., et al. (2012), Prototyping a global soft X-ray imaging instrument for heliophysics, planetary science, and astrophysics science, *Astron. Nachr.*, *333*(4), 378–382, doi:10.1002/asna.201211662.
Cravens, T. E. (1997), Comet Hyakutake X-ray source: Charge transfer of solar wind heavy ions, *Geophys. Res. Lett.*, *24*, 105–108, doi:10.1029/96GL03780.
Cravens, T. E. (2002), X-ray emission in the solar system, in *Atomic Processes in Plasmas: 13th APS Topical Conference on Atomic Processes in Plasmas*, edited by D. R. Schultz et al., pp. 173–181, AIP Conf. Proc. 635, American Institute of Physics, College Park, MD.
Cravens, T. E., I. P. Robertson, and S. L. Snowden (2001), Temporal variations of geocoronal and heliospheric X-ray emission associated with the solar wind interaction with neutrals, *J. Geophys. Res.*, *106*(A11), 24,883–24,892.
Dhanya, M. B., A. Bhardwaj, Y. Futaana, S. Fatemi, M. Holmström, S. Barabash, M. Wieser, P. Wurz, A. Alok, and R. S. Thampi (2013), Proton entry into the near-lunar plasma wake for magnetic field aligned flow, *Geophys. Res. Lett.*, *40*, 2913–2917, doi:10.1002/grl.50617.
Dennerl, K. (2002), Discovery of X-rays from Mars with Chandra, *Astron. Astrophys.*, *394*, 1119–1128, doi:10.1051/0004-6361:20021116.
Dennerl, K. (2008), X-rays from Venus observed with Chandra, *Planet. Space Sci.*, *56*, 1414–1423.
Dennerl, K., V. Burwitz, J. Englhauser, C. Lisse, and S. Wolk (2002), Discovery of X-rays from Venus with Chandra, *Astron. Astrophys.*, *386*, 319–330, doi:10.1051/0004-6361:20020097.
Elphic, R., G. Delory, A. Colaprete, M. Horanyi, P. Mahaffy, B. Hine, D. Harris, J. Salute, E. Grayzeck, and D. Boroson (2011), Status of NASA's Lunar Atmosphere and Dust Environment Explorer (LADEE), Abstract 447 paper presented at NASA Lunar Science Forum, July 19-21, 2011, Ames, California.
Farrell, W. M., T. J. Stubbs, J. S. Halekas, G. T. Delory, M. R. Collier, R. R. Vondrak, and R. P. Lin (2008), Loss of solar wind plasma neutrality and affect on surface potential near the lunar terminator and shadowed polar regions, *Geophys. Res. Lett.*, *35*, L05105, doi:10.1029/2007GL032653.
Fatemi, S., M. Holmström, and Y. Futaana (2012), The effects of lunar surface plasma absorption and solar wind temperature anisotropies on the solar wind proton velocity space distributions in the low-altitude lunar plasma wake, *J. Geophys. Res.*, *117*, A10105, doi:10.1029/2011JA017353.
Fatemi, S., M. Holmström, Y. Futaana, S. Barabash, and C. Lue (2013), The lunar wake current systems, *Geophys. Res. Lett.*, *40*, 17–21, doi:10.1029/2012GL054635.
Feldman, P. D., D. M. Hurley, K. D. Retherford, G. R. Gladstone, S. A. Stern, W. Pryor, J. W. Parker, D. E. Kaufmann, M. W. Davis, and M. H. Versteeg (2012), Temporal variability of lunar exospheric helium during January 2012 from LRO/LAMP, *Icarus*, *221*(2), 854–858, doi:10.1016/j.icarus.2012.09.015.
Freeman, J. W., Jr. (1972), Energetic ion bursts on the nightside of the Moon, *J. Geophys. Res.*, *77*, 239–243.
Freeman, J. W., and M. Ibrahim (1975), Lunar electric fields, surface potential and associated plasma sheaths, *Moon*, *14*, 103–114.
Futaana, Y., S. Barabash, M. Wieser, M. Holmström, A. Bhardwaj, M. B. Dhanya, R. Sridharan, P. Wurz, A. Schaufelberger, and K. Asamura (2010), Protons in the near-lunar wake observed by the sub-keV atom reflection analyzer on board Chandrayaan-1, *J. Geophys. Res.*, *115*, A10248, doi:10.1029/2010JA015264.
Galvin, A. B., et al. (2009), Solar wind ion trends and signatures: STEREO PLASTIC observations approaching solar minimum, *Ann. Geophys.*, *27*, 3909–3922.
Giacconi, R., H. Gursky, F. R. Paolini, and B. B. Rossi (1962), Evidence for X-rays from sources outside the solar system, *Phys. Rev. Lett.*, *9*, 439–443.
Gott, J. R., III, and A. E. Potter Jr. (1970), Lunar atomic hydrogen and its possible detection by scattered Lyman-α radiation, *Icarus*, *13*, 202–206.
Greenwood, J. B., I. D. Williams, S. J. Smith, and A. Chutjian (2000), Measurement of charge exchange and X-ray emission cross sections for solar wind-comet interactions, *Astrophys. J.*, *533*(2), L175–L178, doi:10.1086/312615.
Gunell, H., M. Holmström, E. Kallio, P. Janhunen, and K. Dennerl (2004), X-rays from solar wind charge exchange at Mars: A comparison of simulations and observations, *Geophys. Res. Lett.*, *31*, L22801, doi:10.1029/2004GL020953.
Halekas, J. S., S. D. Bale, D. L. Mitchell, and R. P. Lin (2005), Electrons and magnetic fields in the lunar plasma wake, *J. Geophys. Res.*, *110*, A07222, doi:10.1029/2004JA010991.
Hartle, R. E. (1971), Model for rotating and nonuniform planetary exospheres, *Phys. Fluids*, *14*, 2592–2598, doi:10.1063/1.1693379.
Haymes, R. C., and R. D. Juday (1965), Detectability of lunar X-rays, *Planet. Space Sci.*, *13*, 1249–1254.
Hodges, R. R. (1973), Helium and hydrogen in the lunar atmosphere, *J. Geophys. Res.*, *78*, 8055–8064.
Hodges, R. R. (1975), Formation of the lunar atmosphere, *Moon*, *14*, 139–157.
Hodges, R. R., Jr. (1977), Release of radiogenic gases from the Moon, *Phys. Earth Planet. Inter.*, *14*, 282–288.
Hodges, R. R. (1994), Monte Carlo simulation of the terrestrial hydrogen exosphere, *J. Geophys. Res.*, *99*(A12), 23,229–23,247.
Hodges, R. R. (2011), Resolution of the lunar hydrogen enigma, *Geophys. Res. Lett.*, *38*, L06201, doi:10.1029/2011GL046688.
Holmström, M., and E. Kallio (2004), The solar wind interaction with Venus and Mars: Energetic neutral atom and X-ray imaging, *Adv. Space Res.*, *33*, 187–193.
Holmström, M., S. Barabash, and E. Kallio (2001), X-ray imaging of the solar wind-Mars interaction, *Geophys. Res. Lett.*, *28*, 1287–1290.
Holmström, M., S. Fatemi, Y. Futaana, and H. Nilsson (2012), The interaction between the Moon and the solar wind, *Earth Planets Space*, *64*(2), 237–245, doi:10.5047/eps.2011.06.040.
Hosokawa, K., S. Taguchi, S. Suzuki, M. R. Collier, T. E. Moore, and M. F. Thomsen (2008), Estimation of magnetopause motion from low-energy neutral atom emission, *J. Geophys. Res.*, *113*, A10205, doi:10.1029/2008JA013124.
Ishikawa, K., Y. Ezoe, Y. Miyoshi, N. Terada, K. Mitsuda, and T. Ohashi (2013), Suzaku observation of strong solar-wind charge-exchange emission from the terrestrial exosphere during a geomagnetic storm, *Publ. Astron. Soc. Jpn.*, *65*, 63-1–63-10.
Kallio, E., P. Wurz, R. Killen, S. McKenna-Lawlor, A. Milillo, A. Mura, S. Massetti, S. Orsini, H. Lammer, P. Janhunen, and W.-H. Ip (2008), On the impact of multiply charged heavy solar wind ions on the surface of Mercury, *Planet. Space Sci.*, *56*, 1506–1516.
Kato, M., S. Sasaki, K. Tanaka, Y. Iijima, and Y. Takizawa (2008), The Japanese lunar mission SELENE: Science goals and present status, *Adv. Space Res.*, *42*, 294–300, doi:10.1016/j.asr.2007.03.049.
Killen, R. M., D. M. Hurley, and W. M. Farrell (2012), The effect on the lunar exosphere of a coronal mass ejection passage, *J. Geophys. Res*, *117*, E00K02, doi:10.1029/2011JE004011.

Koutroumpa, D., M. R. Collier, K. D. Kuntz, R. Lallement, and S. L. Snowden (2009), Solar wind charge exchange emission from the helium focusing cone: Model to data comparison, *Astrophys. J.*, *697*, 1214–1225.

Krasnopolsky, V. A., J. B. Greenwood, and P. C. Stancil (2004), X-ray and extreme ultraviolet emissions from comets, *Space Sci. Rev.*, *113*, 271–373.

Kremser, G., W. Stüdemann, B. Wilken, G. Gloeckler, D. C. Hamilton, and F. M. Ipavich (1987), Average spatial distributions of energetic O^+, O^{2+}, O^{6+}, and C^{6+} ions in the magnetosphere observed by AMPTE CCE, *J. Geophys. Res.*, *92*, 4459–4466.

Lisse, C. M., et al. (1996), Discovery of X-ray and extreme ultraviolet emission from comet C/Hyakutake 1996 B2, *Science*, *274*(5285), 205–209.

Lui, A. T. Y. (1987), Road map to magnetotail domains, in *Magnetotail Physics*, pp. 3-9, Johns Hopkins Univ. Press, Baltimore, MD.

Lumb, D. H., R. S. Warwick, M. Page, and A. De Luca (2002), X-ray background measurements with XMM-Newton, *Astron. Astrophys.*, *389*, 93–105, doi:10.1051/0004-6361:20020531.

Mahaffy, P. R., R. R. Hodges, M. Benna, D. N. Harpold, W. K. Kasprzak, J. W. Kellogg, and T. T. King (2009), Neutral mass spectrometer under development for the Lunar Atmosphere and Dust Environment Explorer (LADEE) mission, in *40th Lunar and Planetary Science Conference, March 23-27, 2009, The Woodlands, Texas*, pp. 1217.

Mitchell, D. L., J. S. Halekas, R. P. Lin, S. Frey, L. L. Hood, M. H. Acuña, and A. Binder (2008), Global mapping of lunar crustal magnetic fields by Lunar Prospector, *Icarus*, *194*, 401–409, doi:10.1016/j.icarus.2007.10.027.

Nakagawa, T. (2013), Ion entry into the wake behind a nonmagnetized obstacle in the solar wind: Two-dimensional particle-in-cell simulations, *J. Geophys. Res. Space Physics*, *118*, 1–12, doi:10.1002/jgra.50129.

Neugebauer, M., T. E. Cravens, C. M. Lisse, F. M. Ipavich, D. Christian, R. von Steiger, P. Bochsler, P. D. Shah, and T. P. Armstrong (2000), The relation of temporal variations of soft X-ray emission from comet Hyakutake to variations of ion fluxes in the solar wind, *J. Geophys. Res.*, *105*(A9), 20,949–20,955.

Newbury, J. A. (1996), Electron temperature in the solar wind at 1 AU, *Eos Trans. AGU*, *77*(47), 471.

Ninomiya, S., Y. Yamazaki, T. Azuma, K. Komaki, K. Kuroki, and M. Sekiguchi (1998), Measurements of soft X-rays in collision of slow multiply charged Ar ions with an amorphous C target, *Nucl. Instrum. Methods Phys. Res., Sect. B*, *135*, 82–86.

Nishino, M. N., et al. (2009a), Pairwise energy gain-loss feature of solar wind protons in the near-Moon wake, *Geophys. Res. Lett.*, *36*, L12108, doi:10.1029/2009GL039049.

Nishino, M. N., et al. (2009b), Solar-wind proton access deep into the near-Moon wake, *Geophys. Res. Lett.*, *36*, L16103, doi:10.1029/2009GL039444.

Østgaard, N. S., S. B. Mende, H. U. Frey, G. R. Gladstone, and H. Lauche (2003), Neutral hydrogen density profiles derived from geocoronal imaging, *J. Geophys. Res.*, *108*(A7), 1300, doi:10.1029/2002JA009749.

Pepino, R., et al. (2004), Spectra of the X-ray emission induced in the interaction between the solar wind and the heliospheric gas, *Astrophys. J.*, *617*, 1347, doi:10.1086/425682.

Plucinsky, P. P., S. L. Snowden, U. G. Briel, G. Hasinger, and E. Pfeffermann (1993), An updated calibration of the ROSAT PSPC particle background for the analysis of diffuse and extended sources, *Astrophys. J.*, *418*, 519–531.

Potter, A. E., R. M. Killen, and T. H. Morgan (2000), Variation of lunar sodium during passage of Moon through the Earth's magnetotail, *J. Geophys. Res.*, *105*, 15,073–15,084.

Predehl, P., J. H. M. M. Schmitt, S. L. Snowden, and J. Trümper (1992), A lunar occultation of the dust-scattering halo around GX 5-1 observed with ROSAT, *Science*, *257*, 935–937.

Richardson, J. D., and K. Paularena (2001), Plasma and magnetic field correlations in the solar wind, *J. Geophys. Res.*, *106*, 239–251.

Robertson, I. P., M. R. Collier, T. E. Cravens, and M. C. Fok (2006), X-ray emission from the terrestrial magnetosheath including the cusps, *J. Geophys. Res.*, *111*(A12), A12105, doi:10.1029/2006JA011672.

Robertson, I. P., et al. (2009), Solar wind charge exchange observed through the lunar exosphere, *Geophys. Res. Lett.*, L21102, doi:10.1029/2009GL040834.

Ruciński, D., A. C. Cummings, G. Gloeckler, A. J. Lazarus, E. Möbius, and M. Witte (1996), Ionization processes in the heliosphere—Rates and methods of their determination, *Space Sci. Rev.*, *78*, 73–84.

Saito, Y., et al. (2010), In-flight performance and initial results of plasma energy angle and composition experiment (PACE) on SELENE (Kaguya), *Space Sci. Rev.*, *154*, 265–303, doi:10.1007/s11214-010-9647-x.

Samir, U., K. H. Wright Jr., and N. H. Stone (1983), The expansion of a plasma into a vacuum: Basic phenomena and processes and applications to space plasma physics, *Rev. Geophys. Space Phys.*, *21*, 1631–1646.

Sarantos, M., R. M. Killen, S. A. Surjalal, and J. A. Slavin (2010), Sources of sodium in the lunar exosphere: Modeling using ground-based observations of sodium emission and spacecraft data of the plasma, *Icarus*, *205*, 364–374.

Sarantos, M., R. M. Killen, D. A. Glenar, M. Benna, and T. J. Stubbs (2012), Metallic species, oxygen and silicon in the lunar exosphere: Upper limits and prospects for LADEE measurements, *J. Geophys. Res.*, *117*, A03103, doi:10.1029/2011JA017044.

Schmitt, J. H. M. M., S. L. Snowden, B. Aschenbach, G. Hasinger, E. Pfeffermann, P. Predehl, and J. Trümper (1991), A soft X-ray image of the Moon, *Nature*, *349*, 583–587.

Schneider, H. E., and J. W. Freeman (1975), Energetic lunar nighttime ion events, *Moon*, *14*, 27–33.

Sembay, S., et al. (2012), AXIOM: Advanced X-ray imaging of the magnetosheath, *Astron. Nachr.*, *333*(4), 388–392, doi:10.1002/asna.201211672.

Snowden, S. L., D. McCammon, D. N. Burrows, and J. A. Mendenhall (1994), Analysis procedures for ROSAT XRT/PSPC observations of extended objects and the diffuse background, *Astrophys. J.*, *424*, 714–728.

Snowden, S. L., R. Egger, M. J. Freyberg, D. McCammon, P. P. Plucinsky, W. T. Sanders, J. H. M. M. Schmitt, J. Trümper, and W. Voges (1997), ROSAT survey diffuse X-ray background maps II, *Astrophys. J.*, *485*, 125–135.

Snowden, S. L., R. Egger, D. P. Finkbeiner, M. J. Freyberg, and P. P. Plucinsky (1998), Progress on establishing the spatial distribution of material responsible for the $\frac{1}{4}$ keV soft X-ray diffuse background local and halo components, *Astrophys. J.*, *493*, 715–729.

Snowden, S. L., M. R. Collier, and K. D. Kuntz (2004), XMM-Newton observations of solar wind charge exchange emission, *Astrophys. J.*, *610*, 1182–1190.

Stern, S. A. (1999), The lunar atmosphere: History, status, current problems, and context, *Rev. Geophys.*, *37*(4), 453–491.

Taguchi, S., S. H. Chen, M. R. Collier, T. E. Moore, M. C. Fok, K. Hosokawa, and A. Nakao (2005), Monitoring the high-altitude cusp with the Low Energy Neutral Atom imager: Simultaneous observations from IMAGE and Polar, *J. Geophys. Res.*, *110*, A12204, doi:10.1029/2005JA011075.

Tenishev, V., M. Rubin, O. J. Tucker, M. R. Combi, and M. Sarantos (2013), Kinetic modeling of sodium in the lunar exosphere, *Icarus*, *226*, 1538–1549, doi:10.1016/j.icarus.2013.08.021.

Trümper, J. (1993), ROSAT – A new look at the X-ray sky, *Science*, *260*, 1769–1771.

Von Steiger, R., and T. H. Zurbuchen (2006), Kinetic properties of heavy solar wind ions from Ulysses-SWICS, *Geophys. Res. Lett.*, *33*, L09103, doi:10.1029/2005GL024998.

Wargelin, B. J., M. Markevitch, M. Juda, V. Kharchenko, R. Edgar, and A. Dalgarno (2004), Chandra observations of the "dark" Moon and geocoronal solar wind charge transfer, *Astrophys. J.*, *607*, 596–610.

Wieser, M., S. Barabash, Y. Futaana, M. Holmström, A. Bhardwaj, R. Sridharan, M. B. Dhanya, P. Wurz, A. Schaufelberger, and K. Asamura (2009), Extremely high reflection of solar wind protons as neutral hydrogen atoms from regolith in space, *Planet. Space Sci.*, *57*, 2132–2134.